Supplementary material for

Solid State Pathways to Complex Shape Evolution and Tunable Porosity during Metallic Crystal Growth

Carlos Díaz Valenzuela,[1] Gabino A. Carriedo,[2] María L. Valenzuela,[3] Luis Zúñiga,[4] and Colm O'Dwyer[5,6,7]*

[1] *Departamento de Química, Facultad de Ciencias, Universidad de Chile, Casilla 653, Santiago, Chile*
[2] *Departamento de Química Orgánica e Inorgánica, Facultad de Química, Universidad de Oviedo, C/Julián Clavería S/N, Oviedo 3307, Spain*
[3] *Universidad Andres Bello, Departamento de Ciencias Química, Facultad de Ciencias, Av. Republica 275, Santiago, Chile*
[4] *Departamento de Física, Universidad de Chile, Facultad de Ciencias Físicas y Matemáticas, Blanco Encalada 2008, Santiago, Chile*
[5] *Department of Chemistry, University College Cork, Cork, Ireland*
[6] *Department of Physics and Energy, and Materials and Surface Science Institute, University of Limerick, Limerick, Ireland*
[7] *Micro and Nanoelectronics Centre, Tyndall National Institute, Lee Maltings, Cork, Ireland*

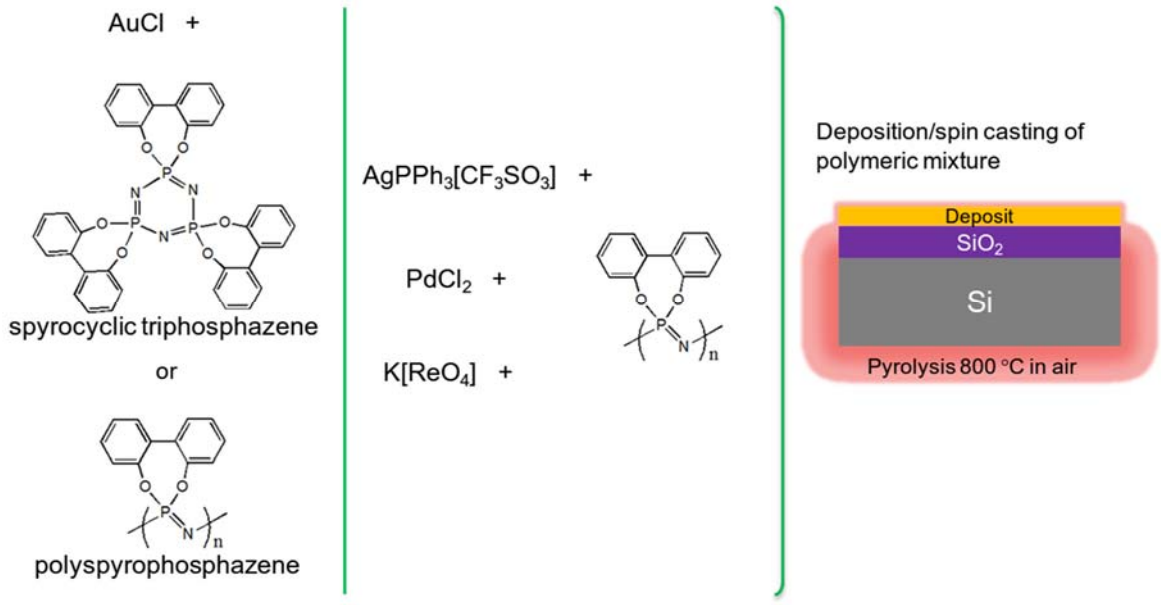

Figure S1. Formulas of the spyrocyclic triphosphazene and the polyspyrophosphazene components of the mixtures with AuCl. Other metallic precursors (middle column) were mixed in 1:1 ratios and pyrolysis is conducted at 800 °C to allow efficient decarbonylation (<300 °C), carbonization at higher temperatures and subsequent elimination of organic matter.

Decomposition mechanism

Confirmation of this mechanism stems from the thermogravimetric and differential scanning calorimetric measurements of the precursor mixtures, shown below in Fig. S2. Several stages of efficient decarbonylation and combustion of organic matter can be clearly monitored and confirmed. The TGA curve for the 1:1 mixture $N_3P_3(O_2C_{12}H_8)_3$/AuCl(PPh_3) exhibits a residue at 800°C of 22.80% which compares well with calculated value of 21.69% corresponding to the Au content. The following three principle weight losses observed correspond to calcination of the organic matter separated for the two organic groups: the first two correspond to the $(O_2C_{12}H_8)_3$ groups, calculated as 45.57% and confirmed from its TGA curve to be 46.57%. The weight loss at 890°C corresponds to the combustion of the Ph_3 groups, calculated as 25.42% and experimentally found to be 22.03%. The DSC characterization agrees, exhibiting three exothermic peaks around 260°C and 275°C and one at 450°C typical of the combustion of the organic matter.(1)

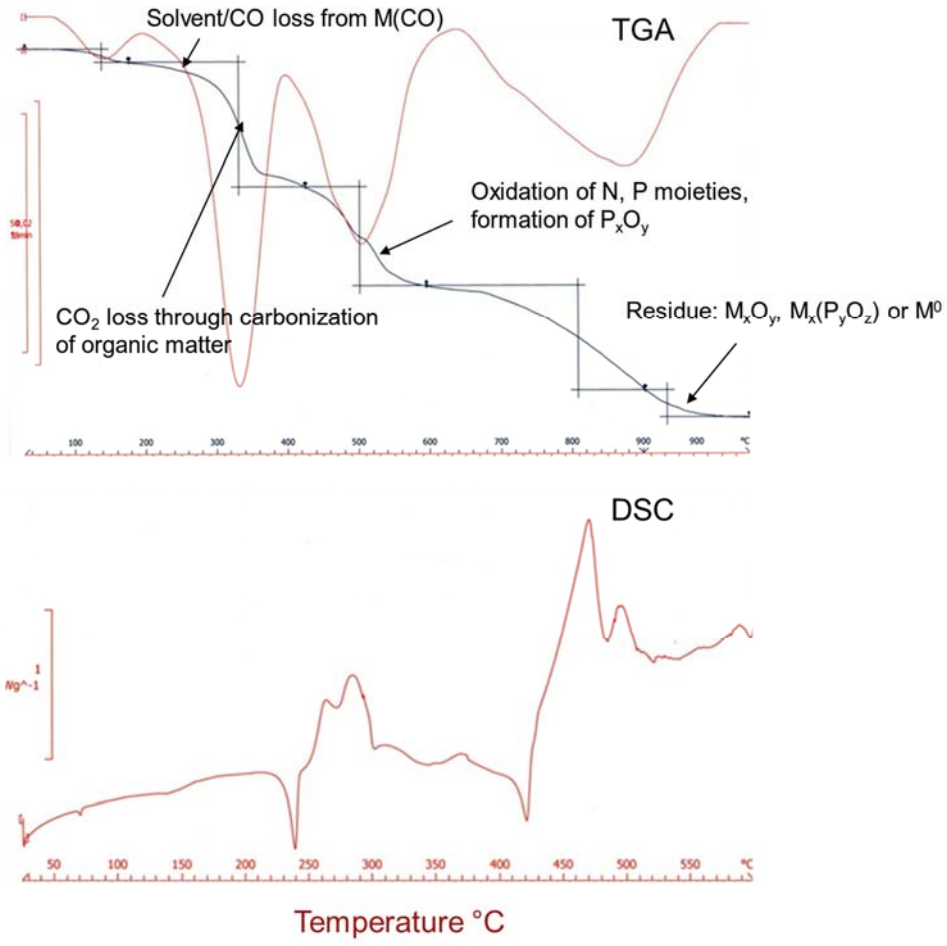

Figure S2. Thermogravimetric analysis and differential scanning colorimetric curves for the pyrolysis of the 1:1 mixture of $N_3P_3(O_2C_{12}H_8)_3$/AuCl(PPh_3).

A schematic model for the general structure of the mixtures and the proposed decomposition mechanism is shown in Fig. S3. For the polymer mixtures containing $[NP(O_2C_{12}H_8)]_n$/AuCl(PPh_3), a similar scheme involving an interaction between the Au centers and the λ^5-dioxydiaryl groups anchored to the polymer is expected. The

macromolecular Au-containing polymers that have a uniform distribution of the Au(I) centers along the polymeric chains facilitate the easy cleavage and migration of the Au atoms favoring the formation of nanoparticles, which subsequently migrate to the pinholes during demixing. In the case of the $N_3P_3(O_2C_{12}H_8)_3$/AuCl(PPh_3) and $[NP(O_2C_{12}H_8)]_n$/AuCl(PPh_3) mixtures, a strong Au-arene interaction (between the AuCl(PPh_3) molecules and the biphenyl rings) allows regular ordering of the Au centers along the $NP(O_2C_{12}H_8)$ groups of the chains of the polymer, or around the cyclic molecules of trimer; FFT analysis confirms a random spatial distribution at low Au densities. Also, the formation of metallic crystals does not require the covalent linking of the organometallic fragment to the polymeric or trimeric phosphazenes.

Chemical decomposition involves the relatively easy loss of Cl to give PPh_3Au^+ species which are known to interact with the π system of the aryl groups of the bispyro of both the polymer and the trimer. These in turn allow a stable solid matrix which is known to be non-volatile in the first stage of the heating (2) allowing the polymeric cyclomatrix to form. Subsequent oxidation of the organic matter as gases (CO, CO_2, NO_2) gives rise to voids within the cyclomatrix where metal NPs initially form from cleaved atoms.

In the case of the $N_3P_3(O_2C_{12}H_8)_3$/AuCl(PPh_3) and $[NP(O_2C_{12}H_8)]_n$/AuCl(PPh_3) mixtures, a strong Au-arene interaction between the AuCl(PPh_3) molecules and the biphenyl rings) could permit a regular ordering of the Au centers along with the $NP(O_2C_{12}H_8)$ groups of the chains of the polymer or around the cyclic molecules of the trimer, schematically represented in the top portion of Fig. S3. Au(I)-arene interactions have been recently discussed by Laguna *et al.*(3) Intermolecular gold-arenes have been reported in the trinuclear complex $[Au_3(p\text{-}tolN{=}COEt)_3]$.(4) Also metal-arene interactions have been observed in the one dimensional array supramolecular structures of the gold(I) complex [Au(CN){2,6-$NC_5H_3(C_6H_4)_2$-C,C'N}].(5) Intramolecular Metal-arene interaction has been also observed in some complexes. Recently strong M-arene M = Au, Ag, Cu interactions have been reported in metal-dialkylbiarylphosphane complexes.(6)

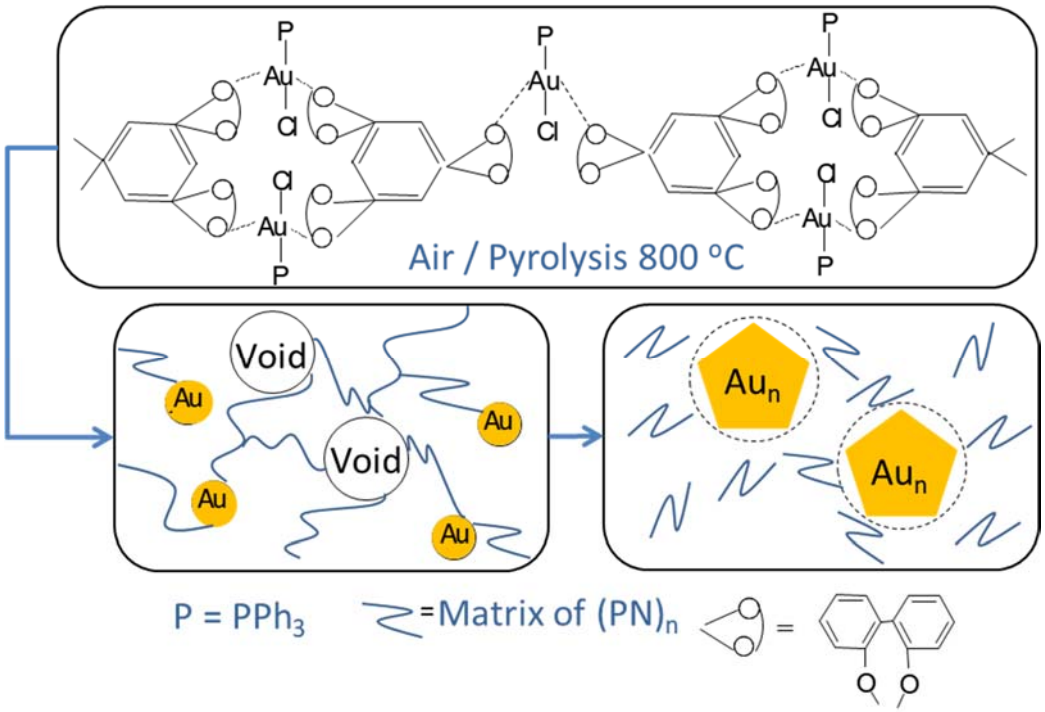

Figure S3. Proposed mechanism of the pyrolysis of a $N_3P_3(O_2C_{12}H_8)_3$/AuCl(PPh_3) mixture as a precursor to metallic crystal formation in the solid state. The overall process applies to Ag, Pd or Re coordinated in a similar way.

Figure S4 shows the NP distribution within the plane of the decomposed metallopolymer, where a random dispersion is found surrounding a nucleation point roughly in the centre. The lighter regions, as outlined in the main text, in this STEM image correspond to the thicker spinodally shaped regions of the polymer. Figure S5 summarises the image analysis method used to obtain the characteristics length scale, *k* and NP statistics. Cluster statistics were only possible for the initial stages of heating, but prior to crystallization as the polymeric material had since carbonized and solidified. Structure factors *S*(k) of the lateral bicontinuous phase were obtained as outlined above.

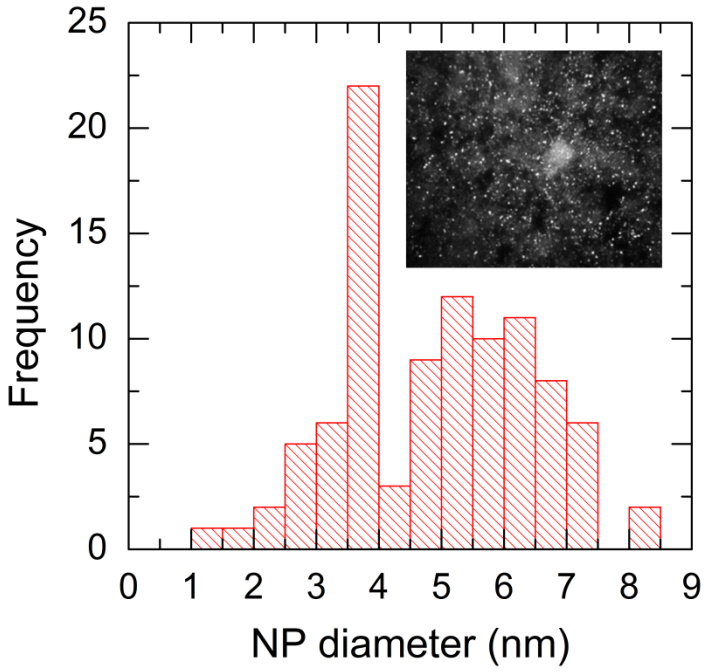

Figure S4. The diameter distribution profile confirms a bimodal Gaussian spread in diameters with 95% of NPs having diameters in the range 3.7-5.5 nm. Inset: Dark field TEM image of gold NPs formed in the demixing polymer mixture. In dark field, the brighter labyrinthine regions constitute the polymer and bright points are the Au NPs.

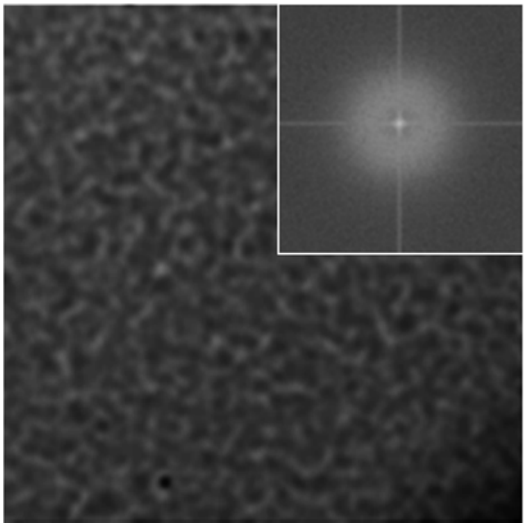

Figure S5. The spinodal character of the 'flat' regions or the carbonized and solidified polymer between pinholes (*cf.* main text, Fig. 1B2). The inset show the power spectrum of the image where a characteristic 'wavelength' of the frozen instability is seen.

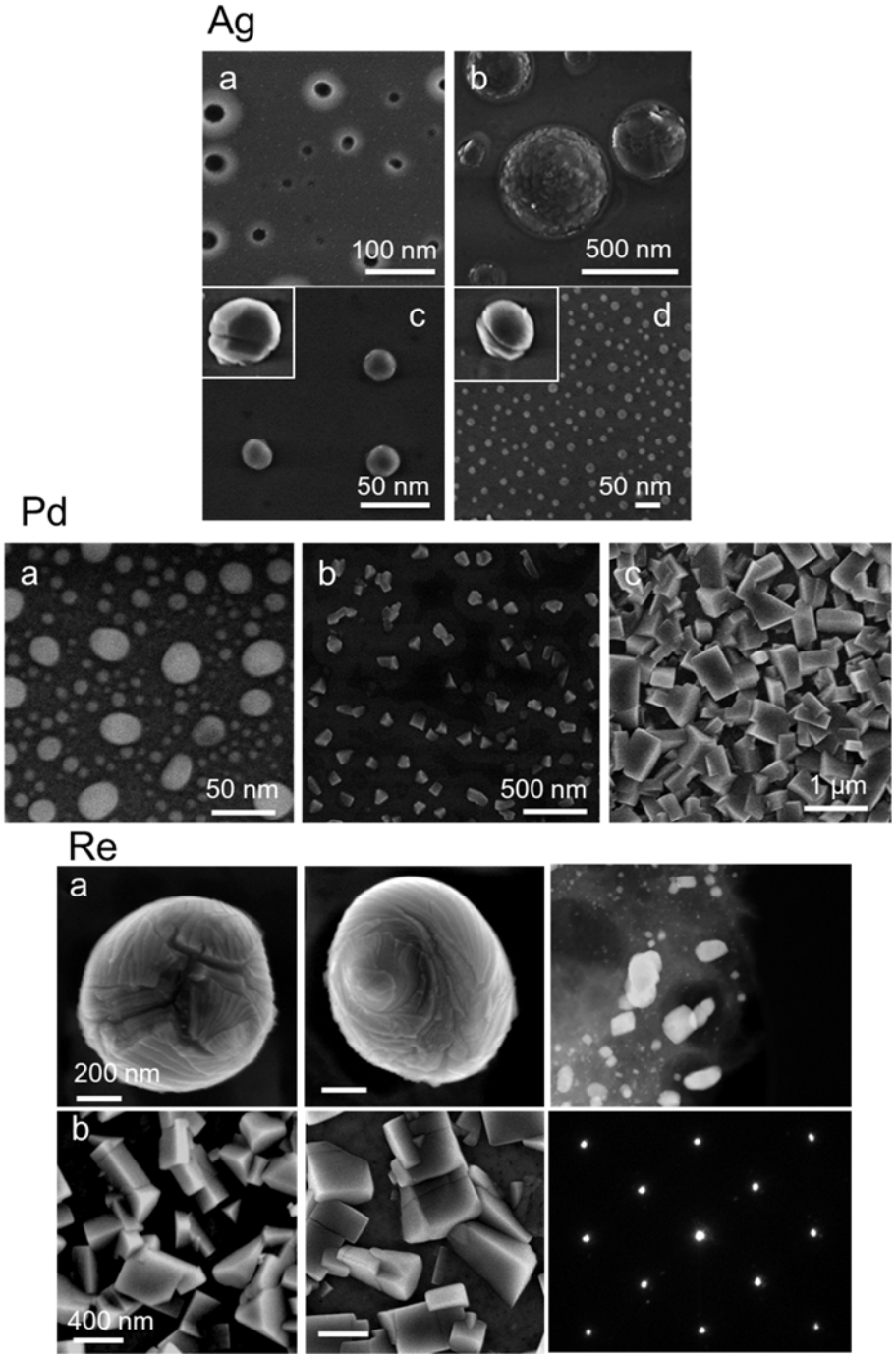

Figure S6. Summary of the salient features of Ag, Pd and Re nano and micro-crystal growth following a similar mechanism to that shown for Au in Figs 1 and 2, main text. Following nucleation dewetting of the polymer and subsequent carbonization and solidification, incubated seeds grown from coarsening NPs around the pinhole rims, leads to continued crystal growth. For Ag, complex shapes are not typically observed. The majority of particles are either faceted, in dumb-bell shapes of pseudo-spherical. For Re and Pd, frustrated cuboidal structures are most common, typically with clipped corners. HR STEM of the Re system confirms coarsening and growth of the crystals deep within the pyrolized matrix (a, right). Thin metallic films have also been shown to dewet under localized heating, and result in essenitaly a solid state dewetting with spinodal instability formation observed (7-9). However, these studies are characteristically different in that there is no organic phase that can liquefy and subsequently solidify which changing chemical composition.

Composition and phase purity of metallic crystals

After oxygen plasma removal of all organic matter at intermediate stages, X-ray photoelectron spectroscopy analysis of a single open topped structure (Fig. S7) confirms uniphasic pure gold where the characteristic doublet of $Au4f_{7/2}$ and $Au4f_{5/2}$ at binding energies of 83.7 and 87.3 eV, are found indicative of Au^0. EDX (see main text) conclusively confirms pure monophasic Au composition of all sizes of crystals formed. EDX analysis was also conducted on Pd and Re crystal and nanoparticles. In Fig. S8, nanoscale resolution EDX confirms pure metallic crystal formation in each case. EDX analysis of Ag crystals was complicated by the presence of a silver phosphate (see Fig. S9) phase surrounding the crystals, but line scan mapping together with C and Ag, conclusively shows that the Ag crystals themselves, are pure crystalline Ag.

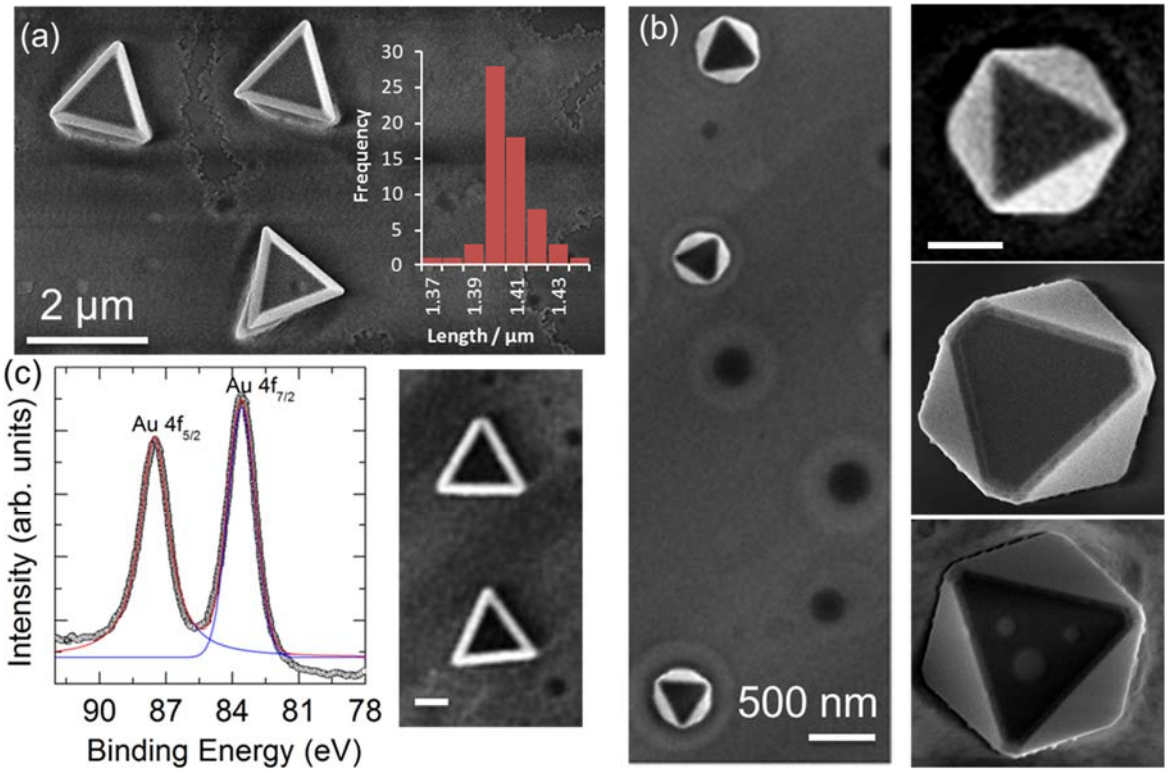

Figure S7. (a) SEM image of intermediate gold tetrahedra grown from pyrolyzed $NP(O_2C_{12}H_8)_n/AuCl(PPh_3)$ 3:1 (1) precursor deposited as a film. The inset shows EDX line scan confirming (apart from carbon) the sole presence of gold. (b) SEM of cuboctahedral gold crystals grown from pinholes in the solid carbonized polymer, each with similar size and shape but grown from pinholes of different diameter. The inset in (a) is the frequency distribution of the consistent edge lengths for tetrahedra. Perfect decahedra also formed on the same length scale. (c) X-ray photoelectron spectroscopy of Au4f core-levels acquired after oxygen plasma etching of organic matter for decahedra and triangular platelets, also confirms purely metallic gold. AFM analysis of the height of a typical tetrahedron gives a mean value of ~1.6 µm, which corresponds to the theoretical height of $\sqrt{(2/3)}a$, where a is the edge length measured to be consistently ~1.4 µm.

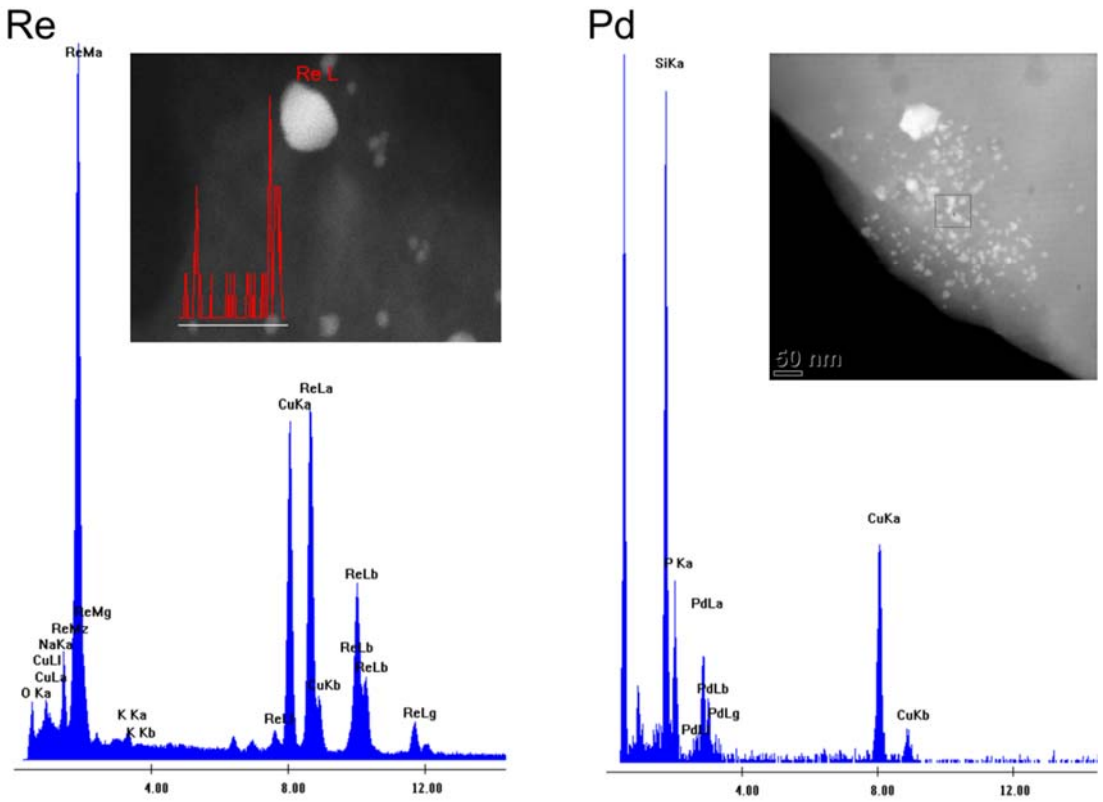

Figure S8. TEM EDX of Re and Pd nanoparticles captured at the early stages of formation, where the phase purity of each is confirmed on the nanoscale, in addition to bulk confirmation from XRD shown in Fig. S9 below. The Cu signals comes from the TEM sample grid and Si surfaces on which samples were deposited.

The phase purity and crystallinity of the gold structures was further confirmed by X-ray diffraction (Fig. S9) where for precursors that form predominantly tetrahedra, a predominance of (111) planes are found in cubic gold; the same applies for Pd and Re. For Ag precursors, the (210), (211), (310) and (222), (322) and (321) typical of cubic Ag_3PO_4 are found. Other less intense peaks at $2\theta = 26 – 28°$ were assigned to the oxide $(P_4O_6)O_2$. Thus the formation of Ag_3PO_4 together with Ag is typical of the solid-state pyrolysis of Ag containing precursors $AgPPh_3[CF_3SO_3]/[NP(O_2C_{12}H_8)]_3$ (10).

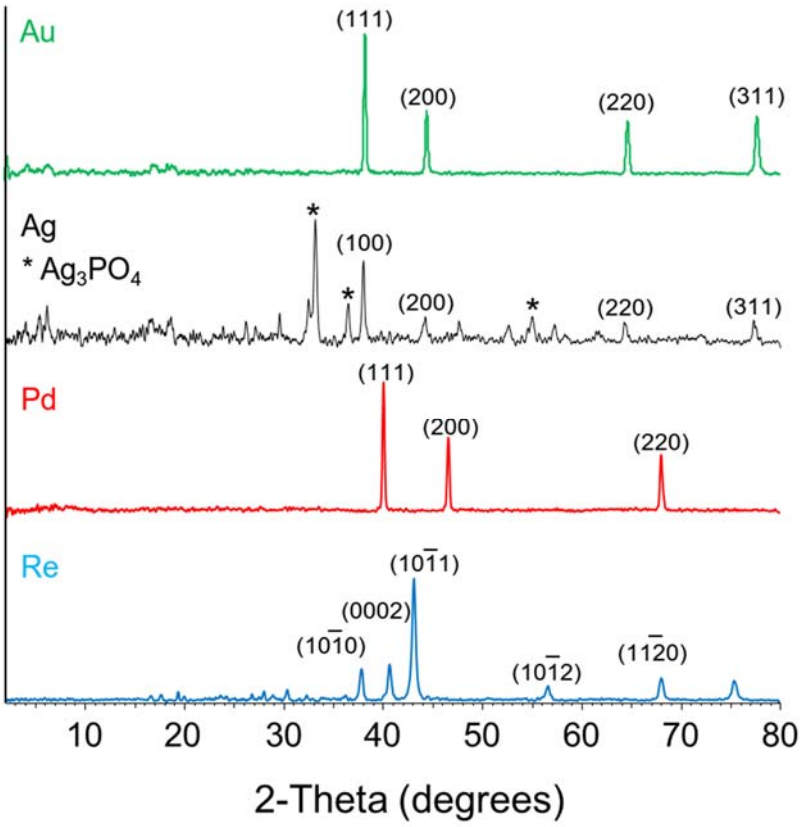

Figure S9. X-ray diffraction pattern of a typical pyrolyzed precursor (3) indexed to cubic gold (JCPDS 4-784) with a clear predominance of (111) reflections consistent with the majority of gold crystals being delineated by {111} planes. The intensities of the (200) and (220) fcc reflections is observed to increase with larger crystal sizes and reduced faceting; {111} planes are predominant on icosahedra and tetrahedra of fcc gold. All the XRD patterns of the investigated samples show the (100), (200), (220) and (311) planes of a fcc lattice of cubic Pd, Au or Ag; Re is a hexagonal structure with space group P63/*mmc* and cell parameters a = 0.276 nm and c = 0.445 nm, (JCPDS #00-001-1231).

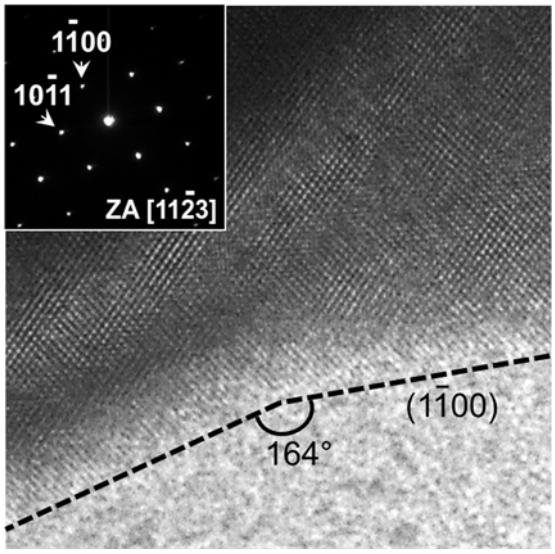

Figure S10. TEM image of the facets formed in 3 nm size single crystal Re NP. In addition to high angle and facet surfaces, we never observe remnant organics or carbonaceous material coating the surfaces of Re crystals, or indeed any of the Ag, Au or Pd crystals.

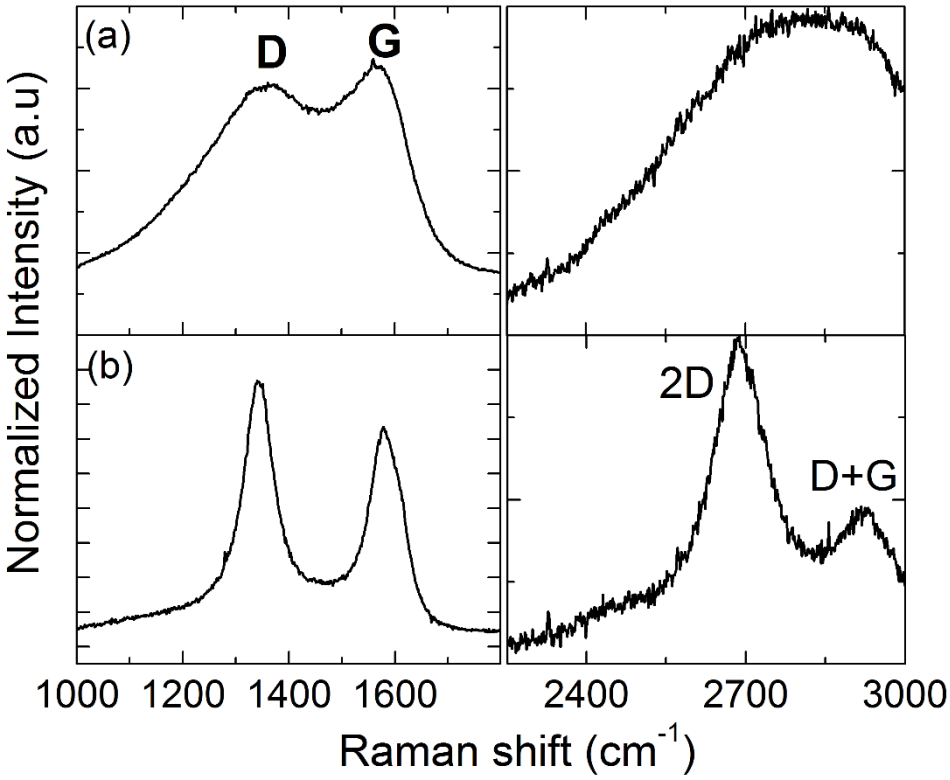

Figure S11. The surface of the carbon matrix from a Re crystal forming complex shows a convoluted D- and G-band pair; convoluted scattered phonon processes describe a mixture of 2D and 3D graphite where the D-band is attributed to curved and disordered graphite sheets and the G-band is characteristic of layered graphite. The micro-Raman spectra from localized regions of NP-free cyclomatrix-like carbon after complete pyrolysis and graphitization confirms higher quality and density of layered graphite. The 2D band correlates to stacking order and number of layered graphene-like sheets where the single-peak 2D band indicates a low number of layers. The D+G band at ~2950 cm^{-1} indicates the support contains very disordered, randomly oriented graphene sheets.

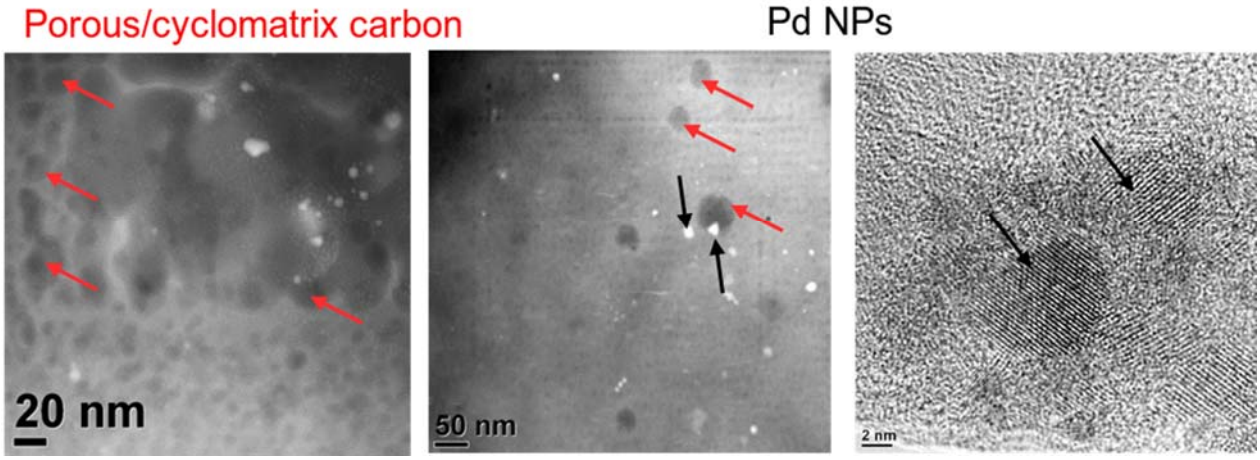

Figure S12. HAADF STEM image of the Pd precursor showing Pd nanocrystal formation (black arrows) and the nucleation of internal cyclomatrix void formation (red arrows) (see Fig. S3) with the carbonized support matrix. HRTEM confirms cyclic, layered graphitic matrix formation during the final annealing step; the method gives the option for NP infiltrated amorphous or graphitic carbons.(11)

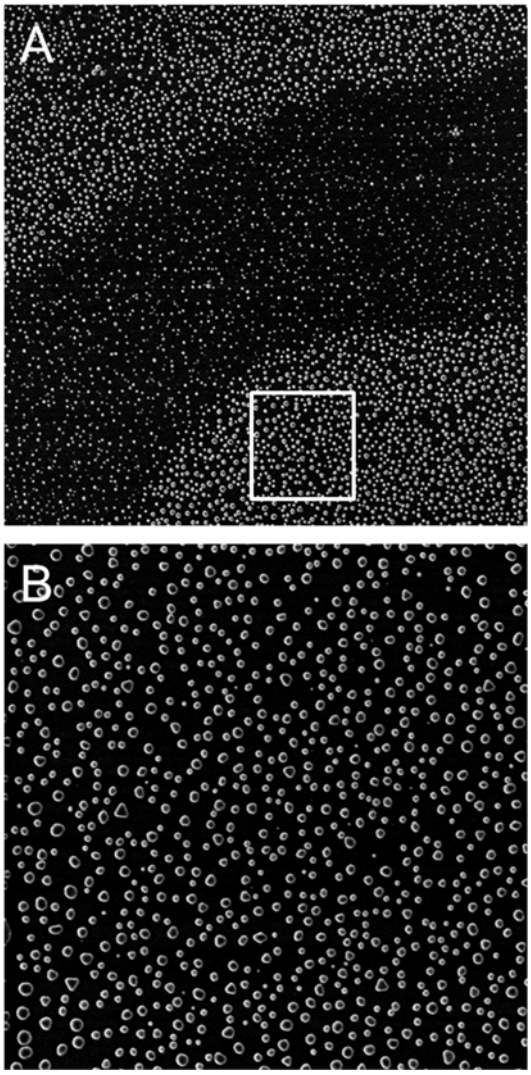

Figure S13. SEM image of pseudo-spherical crystals formed from pyrolysis of a trimer:gold ratio of 3:1. The crystals are random dispersed (see FFT). The density of crystals is dependent on deposition thickness (see main text regarding the formation of various shapes as a function of thickness).

References

(1) Valenzuela, C., Carriedo, G., Luisa Valenzuela, M., Zúñiga, L., O'Dwyer, C. *J. Inorg. Org. Polym. Mater.* **22**, 447 (2012).
(2) Carriedo, G. A., Fernández-Catuxo, L., Alonso, F. J. G., Gómez-Elipe, P. & González, P. A. *Macromolecules* **29**, 5320-5325 (1996).
(3) Rawashdeh-Omary, R. A., Omary, M. A., Fackler, J. P., Galassi, R., Pietroni, B. R., Burini, A. *J. Am. Chem. Soc.* **123**, 9689 (2001).
(4) Laguna, A., in *Modern Supramolecular Gold Chemistry*; Wiley WCH: Wenheim, 2008, Ch. 5, p. 318.
(5) Mohamed, A. A., Rawashdeh-Omary, R. A., Omary, M. A., Fackler, J. P. *Dalton Trans.* 2597 (2005).
(6) Perez-Galan, P., Delpont, N., Guerrero-Gomez, H., Maseras, F., Echavarren, A. M., *Chem. Eur. J.* **16**, 5324 (2010).

(7) Oh, Y.-J., Ross, C. A., Jung, Y. S., Wang, Y. & Thompson, C. V. *Small* **5**, 860 (2009).
(8) Kim, D., Giermann, A. L., Thompson, C. V., *Appl. Phys. Lett.*, **95**, 251903 (2009).
(9) El-Sayed, H. A., Molero, H. M., Birss, V. I., *Nanotechnology*, **23**, 435602 (2012).
(10) Jimenez, J., Laguna, A., Benouazzane, M., Sanz, J. A., Díaz, C., Valenzuela, M. L., Jones, P. G. *Chem. Eur. J.* **15**, 13509 (2009).
(11) Díaz, C., Valenzuela, M. L., Lavayen, V., O'Dwyer, C., *Inorg. Chem.* **51**, 6228 (2012).